3D Reconstruction of the Source and Scale of Buried Young Flood Channels on Mars

Gareth A. Morgan *et al.*

Science **340**, 607 (2013);
DOI: 10.1126/science.1234787

16. C. T. David, *Physiol. Entomol.* **3**, 191 (1978).
17. J. M. Zanker, *Physiol. Entomol.* **13**, 351 (1988).
18. A. J. Bergou, L. Ristroph, J. Guckenheimer, I. Cohen, Z. J. Wang, *Phys. Rev. Lett.* **104**, 148101 (2010).
19. R. Wood, *IEEE Trans. Robot.* **24**, 341 (2008).
20. K. Ma, S. Felton, R. Wood, "Design, fabrication, and modeling of the split actuator microrobotic bee," 2012 IEEE/RSJ International Conference on Intelligent Robots and Systems, Vilamoura, Algarve, Portugal, 7–12 October 2012, pp. 1133–1140.
21. M. Karpelson, G. Wei, R. Wood, "A review of actuation and power electronics options for flapping-wing robotic insects," 2008 IEEE International Conference on Robotics and Automation, Pasadena, CA, USA, 19–23 May 2008, pp. 779–786.
22. R. Wood, E. Steltz, R. Fearing, *Sens. Actuators A Phys.* **119**, 476 (2005).
23. J. Whitney, R. Wood, *J. Fluid Mech.* **660**, 197 (2010).
24. D. L. Altshuler, W. B. Dickson, J. T. Vance, S. P. Roberts, M. H. Dickinson, *Proc. Natl. Acad. Sci. U.S.A.* **102**, 18213 (2005).
25. Materials and methods are available as supplementary materials on *Science* Online.
26. B. Cheng, X. Deng, T. L. Hedrick, *J. Exp. Biol.* **214**, 4092 (2011).
27. M. Abzug, E. Larrabee, *Airplane Stability and Control: A History of the Technologies that Made Aviation Possible* (Cambridge Univ. Press, Cambridge, UK, 2005).
28. B. Finio, N. Pérez-Arancibia, R. Wood, "System identification and linear time-invariant modeling of an insect-sized flapping-wing micro air vehicle," 2011 IEEE/RSJ International Conference on Intelligent Robots and Systems, San Francisco, CA, USA, 25–30 September 2011, pp. 1107–1114.
29. W. Hoburg, R. Tedrake, System identification of post stall aerodynamics for UAV perching. *Proc. AIAA Infotech Aerospace Conf.* (AIAA, Seattle, WA, 2009).
30. M. Oppenheimer, D. Doman, D. Sigthorsson, Dynamics and control of a biomimetic vehicle using biased wingbeat forcing functions: Part I—Aerodynamic model. *Proc. 48th AIAA Aerospace Sci. Meeting* (AIAA, Orlando, FL, 2010).

Acknowledgments: This material is based on work supported by the National Science Foundation under grant CCF-0926148, the Office of Naval Research under grant N00014-08-1-0919, and the Wyss Institute for Biologically Inspired Engineering. Any opinions, findings, and conclusions or recommendations expressed in this material are those of the authors and do not necessarily reflect the views of the National Science Foundation.

Supplementary Materials

www.sciencemag.org/cgi/content/full/340/6132/603/DC1
Materials and Methods
Supplementary Text
Figs. S1 and S2
Table S1
References (*31*, *32*)
Movies S1 and S2

22 October 2012; accepted 12 February 2013
10.1126/science.1231806

3D Reconstruction of the Source and Scale of Buried Young Flood Channels on Mars

Gareth A. Morgan,[1]* Bruce A. Campbell,[1] Lynn M. Carter,[2] Jeffrey J. Plaut,[3] Roger J. Phillips[4]

Outflow channels on Mars are interpreted as the product of gigantic floods due to the catastrophic eruption of groundwater that may also have initiated episodes of climate change. Marte Vallis, the largest of the young martian outflow channels (<500 million years old), is embayed by lava flows that hinder detailed studies and comparisons with older channel systems. Understanding Marte Vallis is essential to our assessment of recent Mars hydrologic activity during a period otherwise considered to be cold and dry. Using data from the Shallow Radar sounder on the Mars Reconnaissance Orbiter, we present a three-dimensional (3D) reconstruction of buried channels on Mars and provide estimates of paleohydrologic parameters. Our work shows that Cerberus Fossae provided the waters that carved Marte Vallis, and it extended an additional 180 kilometers to the east before the emplacement of the younger lava flows. We identified two stages of channel incision and determined that channel depths were more than twice those of previous estimates.

The majority of outflow channels on Mars are attributed to megafloods caused by the catastrophic release of groundwater. The most prominent outflow channels, located around the Chryse Basin, are >1000 km long and are estimated to be Hesperian [~3.7 to 3.1 billion years ago (Ga)] in age (*1*–*3*). Marte Vallis in Elysium Planitia is the largest of the young (late Amazonian: ~0.5 Ga to the present) outflow channels on Mars. The channel system extends over ~1000 km in length and ~100 km in width, making Marte Vallis comparable in scale to the Chryse basin channel systems. Young lava flows have fully embayed the most elevated portions of Marte Vallis, and as a consequence the fundamental characteristics of the channels, including their source, depth, and morphology are less well understood than those of the Hesperian channels (*4*), despite being over 2.6 billion years younger (*5*).

Two possible sources have been proposed for Marte Vallis: water flowing from the Athabasca Valles outflow channel in the west (*4*, *6*, *7*), possibly forming bodies of water such as the putative frozen central Cerberus sea (*8*); and water flowing from a now-buried section of Cerberus Fossae (*5, 6, 9*). It is impossible to resolve which of the above hypotheses are correct from investigations of the surface geology alone. Using data from the Shallow Radar (SHARAD) sounder (*10*, *11*) on the Mars Reconnaissance Orbiter, we present a tomographic visualization of the buried Marte Vallis channels (*12*).

All 58 SHARAD tracks covering the uppermost reaches of Marte Vallis [as identifiable in Mars Orbiter Laser Altimeter (MOLA) gridded data] display multiple reflecting horizons (Fig. 1 and fig. S1). From mapping of the spatial distribution of SHARAD subsurface returns (Figs. 1 and 2), three distinct reflectors have been identified. Two of these reflectors are found extensively across the study area and occupy different depth ranges (*13*), referred to here as L1R (the shallower reflector) and L2R (the deeper reflector). The third reflector, R3, is located only in the southern portion of the region (Fig. 1C).

Radargrams reveal that the northern and southern termini of the R3 reflector dip upward and reconnect with the surface, delineating a discrete facies boundary (Fig. 1A and fig. S1). The R3 reflector is located exclusively below a mapped unit of young volcanics, ACy [(*5*), also mapped as AEc_3 by (*14*)] (Fig. 2C and fig. S2C). This unit is interpreted to be formed of voluminous lava flows <230 million years old (*5*, *14*), suggesting that R3 represents the base of a distinct surficial flow. The bases of young lava flows have also been identified by SHARAD west of Ascraeus Mons (*15*). The northern boundary of R3 shows strong spatial correlation with the boundary between ACy and the older unit ACo [>500 million years old (*5*)] (Fig. 2), implying that the lava embayed the preexisting ACo surface south of Cerberus Fossae and flowed toward the northeast (the dominant slope direction of the present surface). The northern portion of the R3 reflector exhibits prominent depressions, delineating subsurface channels (Fig. 1A). These channel features are ~20 km wide and extend for at least 50 km in a northeast direction. Seen in plan form, the channel features begin abruptly adjacent to one another along an orientation trending from northwest to southeast (Fig. 2C and fig. S3).

We interpret these features to be the highest elevated channels of Marte Vallis (Fig. 3), implying that the lava flow whose base is defined by R3 infilled the channels as the lavas flowed to the northeast. This indicates that the erosion of the outflow channel cut into the original underlying surface of unit ACo before the emplacement of the younger ACy lavas (fig. S4). This sequence of events confirms the young age of Marte Vallis and places the channel formation between the emplacement of units ACo and ACy [10 to 500 million years ago (Ma)], in agreement with (*5*).

The L1R and L2R reflectors are found extensively across the study region, suggesting that they represent regional boundaries between three

[1]Center for Earth and Planetary Studies, Smithsonian Institution, Washington, DC, USA. [2]NASA Goddard Space Flight Center, Greenbelt, MD 20771, USA. [3]Jet Propulsion Laboratory, Pasadena, CA, USA. [4]Planetary Science Directorate, Southwest Research Institute, Boulder, CO, USA.

*Corresponding author. E-mail: morganga@si.edu

bedrock facies (Figs. 1 and 2). Further inspection of the radargrams reveals that both reflectors are punctuated by incisions of varying width (Fig. 1, B and C). These incisions are not random but spatially align to reveal complex networks. We interpret the spatial location of the incisions to represent where channels have been eroded through either one or both of the two bedrock boundaries delineated by L1R and L2R. A similar methodology has been applied to map out buried flood channels on Earth through the use of seismic profiles (*16*). No incisions are observable in L1R and L2R below unit ACo, and most SHARAD tracks reveal reflector incisions that spatially correlate with the boundary of ACo and ACy (Fig. 2). This indicates that the facies boundaries are systematically correlated with ACo. Our interpretation is further corroborated by the surface morphology exhibiting streamlined features (which represent bedrock "islands" between the channels) that are spatially correlated with isolated patches of the bedrock reflectors (Fig. 1, B and C, and Fig. 2). We argue that the teardrop-shaped hills and associated reflectors are remnant sections of the older ACo plains isolated by the erosional formation of the Marte Vallis channels (such streamlined features characterize most outflow channels on Mars) before infilling of the channels by the young ACy lavas.

The channels identified in R3 align with the truncation of the L1R and L2R reflectors (fig. S3), implying that they are part of the same channel network. Many martian outflow channels are sourced in chaos terrain, interpreted to be the result of subsidence from the rapid evacuation of groundwater (*17*). The abrupt opening of the channels as seen in R3 and the lack of any evidence for depressions at their source argue against the existence of chaos terrain at the head of Marte Vallis. Instead, the channel alignment at the source matches the orientation of the Cerberus Fossae graben system to the west (Fig. 3). This, and the absence of observable subsurface channels in the southern portions of R3, strongly support the hypothesis that Cerberus Fossae was the source of the Marte Vallis floods. This allows the position of this now-buried portion of Cerberus Fossae to be inferred and suggests that the fissure previously extended at least ~180 km to the east of its present surface expression (Fig. 3 and fig. S3).

The bed of the channel features cannot be mapped "downstream" beyond the areal extent of the R3 reflector. The sounder signal is increasingly attenuated as the thickness of lava above the buried channel bed increases, so we postulate that the R3 reflector may extend over a larger part of the study region at depths beyond the SHARAD signal-penetration limit. Quantifying the channel erosion north of Cerberus Fossae can be achieved by measuring the extent of the incisions into the L1R and L2R reflectors. The horizontal and vertical position of the reflectors on each side of an incision was recorded and combined with the elevations of the streamlined forms in the MOLA data. Connecting these erosional control points yields an approximation of the buried channel morphology for each radargram. Because of the density of the SHARAD coverage, it was possible to interpolate between neighboring tracks to produce a 3D model of the buried Marte Vallis channels (Fig. 4).

The SHARAD data reveal a complex channel system consisting of a broad ~40-km-wide main channel that is adjacent to a raised bench, 120 km in width and incised by anastomosing channels formed around four streamlined islands. Such morphology is consistent with the majority of martian outflow channels, and the scale is comparable to that of the main channel and associated perched tributaries of the prominent Ares Vallis outflow channel system (Hesperian in age) that flows into the Chryse Basin (*18*). The geomorphic configuration of Marte Vallis implies the the system experienced two phases of erosion: (i) to erode the islands and (ii) to cut the main channel below the level of the perched channels. This also implies that the initial stages of channel formation consisted of small-scale anastomosing patterns before flow was concentrated in a deeper, wider channel, leaving the central islands and smaller channels as perched remnants (Fig. 4, fig. S4, and supplementary text). Recent work citing the turbulent nature of the young Elysium Planitia lavas suggests that lava flows may have partially or fully eroded the outflow channels (*19, 20*). Although they are filled with later lavas, our tomographic models show that the Marte Vallis channels are morphologically similar to the circum-Chryse outflow channels, and thus could reasonably have been carved entirely by water.

Estimates of the depth of the channels from time-delay offsets to the surface echo are based on an assumed range of values for the permittivity of the material overlying the L1R and L2R

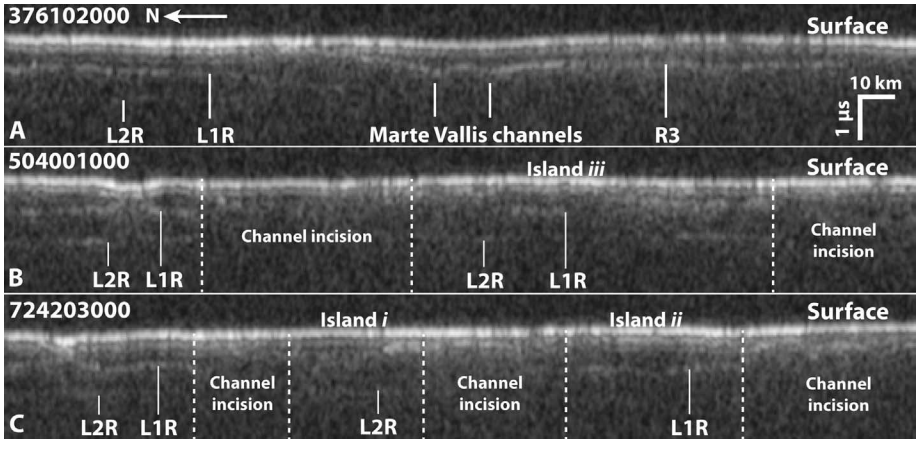

Fig. 1. SHARAD radargrams display the time delay of the echo signal against along-track distance. Subsurface contrasts in permittivity reflect the transmitted signal, producing the observed reflectors. Spatial coordinates of the radargram sections presented are as follows: (**A**) 376102000 (8.42°N, 175.61°E to 4.07°N, 175.08°E), (**B**) 504001000 (10.13°N, 177.81°E to 5.78°N, 177.28°E), (**C**) 724203000 (9.45°N, 176.79°E to 5.1°N, 176.26°E). The locations of the SHARAD tracks are presented in Fig. 2.

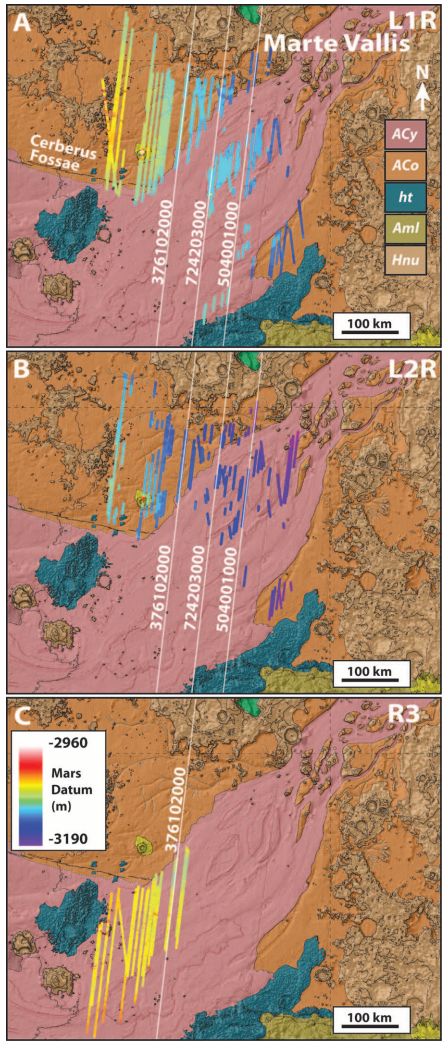

Fig. 2. Spatial distribution of L1R (A), L2R (B), and R3 (C) reflectors corrected for depth (*13*). The background shows the (*5*) geologic map above a hillshade image of MOLA gridded data (200 × vertical exaggeration). ht, hackly terrains; Aml, Medusae Fossae Formation; Hnu, undivided material forming hills and knobs. [Geologic map adapted from (*5*) with permission from Elsevier]

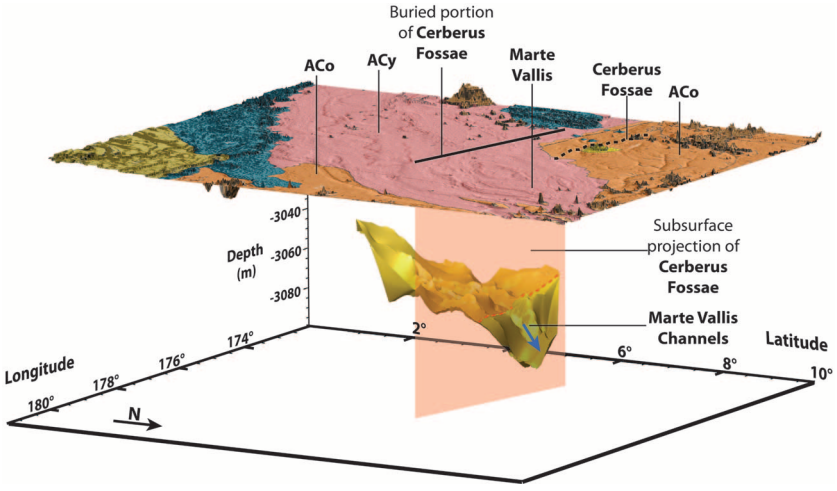

Fig. 3. 3D visualization of the R3 reflector [corrected for depth (*13*)] below the MOLA surface overlain with geologic units (*5*). The surface has been elevated and scaled by a factor of 1/150 for clarity. The Marte Vallis channels are visible as prominent depressions in the R3 reflector and begin abruptly along an orientation that aligns with the subsurface vertical projection of Cerberus Fossae. The blue arrow highlights the direction of flow in the channels. [Geologic map adapted from (*5*) with permission from Elsevier]

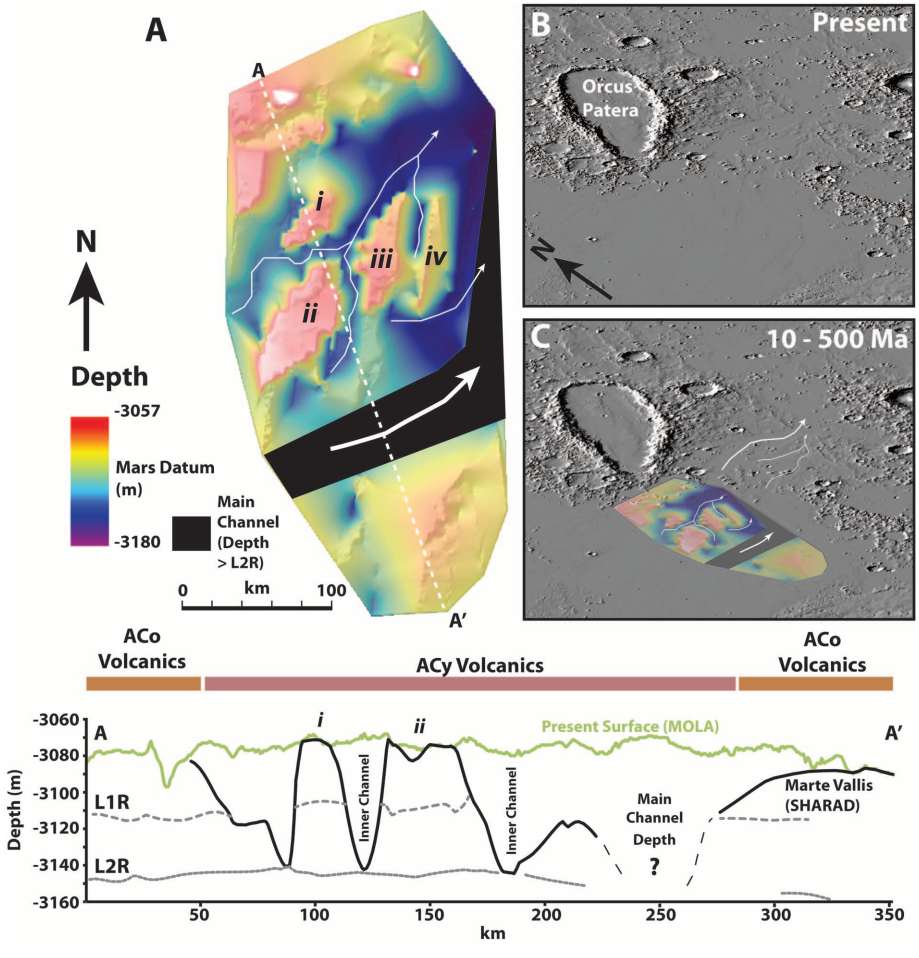

Fig. 4. (A) Tomographic model of the buried Marte Vallis channels and associated NW-SE topographic and tomographic profile (*13*). The model shows an ~40-km-wide main channel and adjacent teardrop-shaped islands. (**B** and **C**) show a perspective view of eastern Elysium Planitia at present (B) and before embayment by young lavas (C). White arrows represent the direction of flow.

reflectors (*21*). The permittivity of these materials is uncertain, but the typical range for dry geological materials is 3 to 8 (*22*, *23*), with lower values leading to greater depths below the surface for any given time delay. For example, the depth of the perched channel between islands ii and iii is constrained between the incised L1R and the continuous L2R reflectors. Applying a permittivity range of 8 to 3 yields a depth range of 35 to 56 m (L1R), to 67 to 110 m (L2R), respectively. With regard to the main channel, the depth estimate (between island i and the south bank) is 69 to 113 m. This is comparable to the depth of incision of the largest known megaflood on Earth, the Missoula floods, responsible for carving the Channeled Scabland of the northwestern United States (*24*). However, the Marte Vallis estimate represents a minimum value, because the L2R reflector has been fully bisected by this channel. The depths of the channels are at least double the previous maximum estimates for Marte Vallis of 40 m (*5*), demonstrating that the scale of the floods has been underestimated.

References and Notes

1. D. H. Scott, K. L. Tanaka, *Geological Map of the Western Equatorial Region of Mars. U.S. Geological Survey Miscellaneous Map I-1802-A* (U.S. Geological Survey, Washington, DC, 1986).
2. K. L. Tanaka, *J. Geophys. Res.* **91**, E139 (1986).
3. S. Rotto, K. L. Tanaka, *Geologic/Geomorphic Map of the Chryse Planitia Region of Mars. U.S. Geological Survey Miscellaneous Investigations Map I-2441* (U.S. Geological Survey, Washington, DC, 1995).
4. D. C. Berman, W. K. Hartmann, *Icarus* **159**, 1 (2002).
5. J. Vaucher *et al.*, *Icarus* **204**, 418 (2009).
6. D. M. Burr, J. A. Grier, A. S. McEwan, L. P. Keszthelyi, *Icarus* **159**, 53 (2002).
7. E. R. Fuller, J. W. Head, *J. Geophys. Res.* **107**, 5081 (2002).
8. J. B. Murray *et al.*; HRSC Co-Investigator Team, *Nature* **434**, 352 (2005).
9. J. B. Plescia, *Icarus* **164**, 79 (2003).
10. R. Seu *et al.*, *Planet. Space Sci.* **52**, 157 (2004).
11. R. Seu *et al.*, *J. Geophys. Res.* **112**, E05S05 (2007).
12. Materials and methods are available as supplementary materials on *Science* Online.
13. The time delay offset between a reflector and the surface echo within a radargram can be converted to depth. This depth estimation is inversely proportional to the square root of the assumed permittivity (ε′) of the material above the reflector. Figures 2 to 4 assume an ε′ of 8, consistent with dense, dry, terrestrial lava flows. Applying a lower value for ε′ would provide a greater depth estimate for each of the reflectors.
14. K. L. Tanaka, J. A. Skinner, T. M. Hare, *Geologic Map of the Northern Plains of Mars, U.S. Geological Survey Scicientific Investigations Map 2888* (U.S. Geological Survey, Washington, DC, 2005).
15. L. M. Carter *et al.*, *Geophys. Res. Lett.* **36**, L23204 (2009).
16. C. S. Fulthorpe, J. A. Austin Jr., *Geology* **32**, 1013 (2004).
17. M. Carr, *J. Geophys. Res.* **84**, 2995 (1979).
18. N. H. Warner, S. Gupta, J.-P. Muller, J.-R. Kim, S.-Y. Lin, *Earth Planet. Sci. Lett.* **288**, 58 (2009).
19. W. L. Jaeger *et al.*, *Icarus* **205**, 230 (2010).
20. D. W. Leverington, *Geomorphology* **132**, 51 (2011).
21. B. A. Campbell *et al.*, *J. Geophys. Res.* **113**, E12010 (2008).
22. F. T. Ulaby *et al.*, *Microwave Dielectric Spectrum of Rocks* (Report 23817-1-T, Univ. of Michigan Radiation Laboratory, Ann Arbor, MI, 1988).
23. W. D. Carrier, G. R. Ohloeft, W. Mendell, Physical properties of the lunar surface, in *Lunar Sourcebook*, G. H. Heiken, D. T. Vaniman, B. M. French, Eds. (Cambridge Univ. Press, New York, 1991), pp. 457–567.

24. V. R. Baker, D. Nummedal, Eds., *The Channeled Scabland; a Guide to the Geomorphology of the Columbia Basin* (NASA, Washington, DC, 1978).

Acknowledgments: C. Chazen and T. Watters provided very helpful reviews of earlier versions of the paper. Comments and suggestions by four anonymous referees were extremely beneficial. Thanks are also extended to P. Russell for his technical assistance. Funding for this work was provided by the NASA Mars Reconnaissance Orbiter Project. The SHARAD data and MOLA altimetry are available through NASA's Planetary Data system.

Supplementary Materials

www.sciencemag.org/cgi/content/full/science.1234787/DC1
Materials and Methods
Supplementary Text
Figs. S1 to S4
Table S1
Reference (*25*)

4 January 2013; accepted 18 February 2013
Published online 7 March 2013;
10.1126/science.1234787

Structural Basis for Molecular Recognition at Serotonin Receptors

Chong Wang,[1]* Yi Jiang,[1,2]* Jinming Ma,[1,3]* Huixian Wu,[1] Daniel Wacker,[1] Vsevolod Katritch,[1] Gye Won Han,[1] Wei Liu,[1] Xi-Ping Huang,[4] Eyal Vardy,[4] John D. McCorvy,[4] Xiang Gao,[3] X. Edward Zhou,[3] Karsten Melcher,[3] Chenghai Zhang,[2,3] Fang Bai,[5] Huaiyu Yang,[6] Linlin Yang,[6] Hualiang Jiang,[6] Bryan L. Roth,[4] Vadim Cherezov,[1] Raymond C. Stevens,[1]† H. Eric Xu[2,3]†

Serotonin or 5-hydroxytryptamine (5-HT) regulates a wide spectrum of human physiology through the 5-HT receptor family. We report the crystal structures of the human 5-HT_{1B} G protein–coupled receptor bound to the agonist antimigraine medications ergotamine and dihydroergotamine. The structures reveal similar binding modes for these ligands, which occupy the orthosteric pocket and an extended binding pocket close to the extracellular loops. The orthosteric pocket is formed by residues conserved in the 5-HT receptor family, clarifying the family-wide agonist activity of 5-HT. Compared with the structure of the 5-HT_{2B} receptor, the 5-HT_{1B} receptor displays a 3 angstrom outward shift at the extracellular end of helix V, resulting in a more open extended pocket that explains subtype selectivity. Together with docking and mutagenesis studies, these structures provide a comprehensive structural basis for understanding receptor-ligand interactions and designing subtype-selective serotonergic drugs.

The neuromodulator serotonin [5-hydroxytryptamine (5-HT)] is essential for diverse functions at nearly every organ system in the human body (*1*–*4*). The activity of 5-HT is mediated through activation of members of a large family of 5-HT receptor proteins that can be grouped into seven subfamilies (5-HT_{1-7}) on the basis of sequence homology and signaling mechanisms (*5*). Except for the 5-HT_3 receptor, which is a ligand-gated ion channel, the other 12 members are heterotrimeric guanine nucleotide binding protein (G protein)–coupled receptors (GPCRs). The serotonergic system is a target of many widely prescribed drugs, including atypical antipsychotics, antimigraine medications, anxiolytics, and antidepressants (*1*), and the recently approved antiobesity medication lorcaserin (*6*, *7*). However, clinical use of several serotonergic drugs caused unexpected side effects arising from off-target interactions with 5-HT receptor subtypes and related receptors for biogenic amine (*1*, *4*, *8*, *9*).

The 5-HT_{1B} receptor couples to G protein alpha subunits G_i or G_o and is widely expressed in the brain and the cardiovascular system. In the CNS, the 5-HT_{1B} receptor functions as an inhibitory presynaptic receptor to modulate the release of 5-HT and many other neurotransmitters (*1*, *2*). The 5-HT_{1B} receptor is a primary molecular target for the antimigraine drugs ergotamine (ERG) and dihydroergotamine (DHE), which are efficacious 5-HT_{1B} receptor agonists (*10*). Off-target activation of the related 5-HT_{2B} receptor is responsible for the valvulopathic activity of many approved drugs and is the main reason for their withdrawal (*9*–*12*). We report two crystal structures of the human 5-HT_{1B} receptor bound to the full agonists, ERG and DHE (tables S1 and S2). Comparison with the structure of the human 5-HT_{2B} receptor bound to ERG (*13*) reveals critical structural determinants for ligand recognition and subtype selectivity and provides a structural rationale for designing safer and more effective serotonergic drugs.

Crystallization studies of the 5-HT_{1B} receptor were done with engineered constructs, 5-HT_{1B}-1 and 5-HT_{1B}-2 (*14*), which crystallized with ERG and DHE at resolutions of 2.7 Å and 2.8 Å, respectively. Due to the high similarity between these two structures (fig. S2), for brevity we focus on the structure of the 5-HT_{1B}-1/ERG complex for analysis and discussion of key structural features for ligand recognition and selectivity in 5-HT_{1B} versus 5-HT_{2B} receptors.

The main fold of the 5-HT_{1B} receptor consists of a canonical seven-transmembrane (7TM) α-helical bundle (Fig. 1A). The extracellular loop 2 (ECL2) that partially covers the ligand binding pocket is stabilized by a $C122^{3.25}$-$C199^{ECL2}$ disulfide bond, highly conserved in GPCRs. Part of the N terminus folds on top of the binding pocket, where Y40 forms hydrogen-bond interactions with ligand binding residue $D352^{7.36}$ (fig. S5) (*15*, *16*). This feature suggests that the N terminus could have a role in ligand recognition in the 5-HT_{1B} receptor by interacting with residues within the binding pocket.

The 5-HT_{1B}/ERG complex structure revealed a large ligand binding cavity defined by residues from helices III, V, VI, VII, and ECL2, comprising an orthosteric pocket embedded deep in the 7TM core and an extended binding pocket close to the extracellular entrance (Fig. 1). ERG adopts a binding mode with the ergoline ring system occupying the orthosteric binding pocket and the cyclic tripeptide moiety bound to the upper extended binding pocket (Fig. 2C). In the orthosteric pocket, the ergoline scaffold is anchored through the salt-bridge interaction between its positively charged nitrogen and the carboxylate of $D129^{3.32}$, which is fully conserved in 5-HT and other monoamine receptors. The side chain of $D129^{3.32}$ is further stabilized by a hydrogen bond to the hydroxyl of $Y359^{7.43}$. Side chains of $C133^{3.36}$, $I130^{3.33}$, $W327^{6.48}$, $F330^{6.51}$, and $F331^{6.52}$ form a narrow hydrophobic cleft, which packs tightly against the nearly planar ergoline ring system. In addition, the indole N-H hydrogen forms a hydrogen bond with $T134^{3.37}$ (Fig. 2A). Comparison with the ERG-bound 5-HT_{2B} receptor structure revealed that the orthosteric binding pockets in the two receptors are very similar, with the key interactions conserved (Fig. 2, A, D, and E). The only difference is observed in the region where residues from helix V contact ERG. Due to the lack of a side chain at $G221^{5.42}$, the side chain of $F217^{5.38}$ in the 5-HT_{2B} receptor reaches into the ligand binding pocket and packs on top of the ERG indole ring; by comparison, the corresponding interaction in the 5-HT_{1B} receptor occurs between the side chain of $S212^{5.42}$ and ERG, whereas $Y208^{5.38}$ does not interact with the ligand due to the outward shift of helix V (Fig. 2, A and D). Substantial differences are observed in the extended

[1]Department of Integrative Structural and Computational Biology, The Scripps Research Institute, 10550 North Torrey Pines Road, La Jolla, CA 92037, USA. [2]Van Andel Research Institute/Shanghai Institute of Materia Medica Center, CAS-Key Laboratory of Receptor Research, Shanghai Institute of Materia Medica, Chinese Academy of Sciences, Shanghai 201203, China. [3]Laboratory of Structural Sciences, Van Andel Research Institute, 333 Bostwick Avenue Northeast, Grand Rapids, MI 49503, USA. [4]National Institute of Mental Health Psychoactive Drug Screening Program, Department of Pharmacology and Division of Chemical Biology and Medicinal Chemistry, University of North Carolina Chapel Hill Medical School, Chapel Hill, NC 27599, USA. [5]Department of Engineering Mechanics, State Key Laboratory of Technology, Faculty of Chemical, Environmental, and Biological Science and Technology, Dalian University of Technology, Dalian 116023, China. [6]State Key Laboratory of Drug Research, Shanghai Institute of Materia Medica, Chinese Academy of Sciences, Shanghai 201203, China.

*These authors contributed equally to this work.
†Corresponding author. E-mail: eric.xu@vai.org (H.E.X); stevens@scripps.edu (R.C.S.)